Sprayed tungsten-doped and undoped bismuth ferrite nanostructured films for reducing and oxidizing gas sensor applications

Shivaji D. Waghmare[a,b], Vijaykumar V. Jadhav[b,c,d], Shoyebmohamad F. Shaikh[b], Rajaram S. Mane[b,*], Jae Hui Rhee[e], Colm O'Dwyer[d,f]

[a] *Department of Physics, Shri. Shivaji Mahavidyalaya, Barshi, Solapur, India*
[b] *Center for Nanomaterials & Energy Devices, School of Physical Sciences, Swami Ramanand Teerth Marathwada University, Nanded 431606, M.S., India*
[c] *Department of Physics, Shivaji Mahavidyalaya, Udgir, Latur, India*
[d] *School of Chemistry, University College Cork, Cork T12 YN60, Ireland*
[e] *Global Frontier Hybrid Interface Materials, Busan, South Korea*
[f] *Micro-Nano Systems Centre, Tyndall National Institute, Lee Maltings, T12 R5CP Cork, Ireland*

Abstract

This work reports the chemical spray synthesis of bismuth ferrite ($BiFeO_3$, abbreviated as BFO) and tungsten-doped bismuth ferrite (W-$BiFeO_3$, abbreviated as BWFO) nanostructured films and their nitro- gen dioxide (NO_2) and hydrogen (H_2) gas sensor applications. The influence of tungsten-doping on the structure, morphology, surface area, and the characteristics towards NO_2 and H_2 gas sensing of BFO has been studied and explored and also compared with pristine BFO. The W-doping in BFO, confirmed by X-ray diffraction, energy dispersive X-ray and Fourier-transform infrared spectroscopy measurements, is proposed to explain the relative improvement in gas sensing performance between BFO and BWFO nanostructured films. At dilute concentration (100 ppm) of NO_2 and H_2, BWFO displays an enhanced sensitivity over BFO, which is attributed to specific changes in the morphology, structure and surface area.

1. Introduction

Metal oxide semiconductor (MOS) gas sensors have been stud- ied extensively and are used practically in various fields [1,2]. In view of the advantages of low-cost, simplicity of use and large num- ber of gases available that require detection, such as inflammable gases [3], hazardous nitrogen dioxide (NO_2) and hydrogen (H_2) [4] and other environmental gases [5], metal oxide-based sensing materials have attracted considerable interest. The working mecha- nism of most metal-oxide semiconductor (MOS)-based gas sensors relies on the sensitive variations to the electrical conductivity of the sensing channel layer [6,7], controlled by a gate voltage in a device with field-effect transistor geometry. Many MOS materials includ- ing ZnO, SnO_2, In_2O_3, WO_3, CuO, and Fe_2O_3, etc., have been studied widely as gas-sensing materials [8,9]. To-date, a range of synthesis methods has been developed to achieve MOS in film and/or pow- der forms with various morphologies and dimensions for sensing applications [10–12], often tuned to maximize surface sensitivity or functional porosity to certain gases, but deposited in a manner that makes MOS structure fabrication feasible. MOS-based sensors have been reported to detect various gases, including H_2 [13], CO [14,15], NH_3 [16], NO_x [17] and organic vapors [18–21], but sensitivity and stability (electrical and environmental) still require updating. MOS sensors still have serious limitations for high temperature gases and, importantly, good selectivity from gas mixtures, particularly using simpler oxides [22].

Bismuth ferrite ($BiFeO_3$, abbreviated as BFO) is one of the most promising MOSs with several prototypical multifunctional properties that are of great technological and fundamental importance [23]. The crystallographic structure of BFO is still discussed controversially in the literature. Some agreement appears to be made on the rhombohedral-distorted perovskite structure (ABO_3, where A and B cations of different charges) [24]. Many studies have reported the synthesis of BFO nanostructures for various applications [5]. Several deposition methods have been envisaged to grow BFO films/powders. Physical deposition methods, such as solid-state [25,26], pulsed laser deposition [27–29], molecular beam epi- taxy [30] and sputtering [31,32], sol-gel, [33,34], co-precipitation [35,36] and hydrothermal methods [37,38] have been applied to the synthesis of BFO films with various morphologies. In addition, there are few reports on the doping and applications of other elements with BFO [39–41] where researchers are optimistic about improv- ing the physical and chemical properties of BFO by substitutional doping with various elements to modify electronic properties. Tungsten (W) is a refractory metal that has shown good response in gas sensing applications specifically at higher temperatures in the trioxide form, such as WO_3 [42–44].

NO_2 and H_2 gases are hazardous and their direct effects on the human body [4] can be harmful. The impact on the health and environment depends on their concentration, exposure time and individual susceptibility. In particular, NO_2 is a by-product of the oxidation reaction of nitrogen in many industrial processes, automotive engines, fossil fuel combustion, and power generating sources [45,46], and is produced in huge amount every year. On the other hand, H_2 is among the most promising clean and renew- able energy resources that can help overcome some of the critical problems related to the depletion of fossil fuel resources, pollution and global warming [47,48]. Recently, the widespread use of H_2 gas in aircraft, internal combustion engines in automobiles, fuel cells, chemical industries (H_2 is a colorless, odorless, highly volatile and inflammable gas when its concentration exceeds 4% in dry air) [48] may possess serious risks associated with its production, storage and uses [49]. Therefore, the development of high performance NO_2 and H_2 sensors is essential for industrial and environmental applications to the formation of potentially explosive mixtures with air which would avoid the risks of explosion and fires.

This paper reports the chemical spray synthesis and NO_2 and H_2 gas sensor applications of BFO and BWFO (tungsten-doped BFO) nanostructured films. The influence of the structure, morphology, crystallite size, surface area on the NO_2 and H_2 sensing properties of BFO, and W-doped sensor films are investigated and reported.

2. Experimental details

2.1. *Synthesis of BFO and BWFO*

All chemicals were of analytical grade and used as received. The BFO and BWFO nanostructured films were synthesized using a chemical spray unit under closed environmental conditions *i.e*. under air-tight conditions involving a two-step synthetic method. For the synthesis of BFO films, 0.2 M bismuth (III) nitrate pentahydrate ($Bi(NO_3)_3{\cdot}5H_2O$), 0.2 M iron(III) nitrate ($Fe(NO_3)_3{\cdot}9H_2O$) and 0.2 M citric acid ($C_6H_8O_7$) were dissolved in double distilled water ($Bi(NO_3)_3{\cdot}5H_2O$ was initially dissolved in nitric acid), and subsequently, a 15 ml solution was ready to spray. Second, 0.2 M sodium tungstate dehydrate ($Na_2WO_4{\cdot}2H_2O$) was added into a previous solution while synthesizing the BWFO film. In the later stage, these solutions were sprayed separately onto non-conducting glass substrate at 400 °C and then the deposited films were air- annealed separately at 500 °C for 4 h. After natural cooling to room-temperature (300K), they were removed and characterized for the electrical resistance, structure and morphology analyses.

2.2. *Characterization details*

The X-ray powder diffraction (XRD, Rigaku D/max--*y* B) patterns were obtained using a Cu K_a radiation source (*A* = 0.15418 nm) operated at 40 kV and 80 mA. Field-emission scanning electron microscopy (FE-SEM, Nova NanoSEM200-100 FEI) images were measured. The chemical composition was elucidated from the energy dispersive X-ray analysis (EDX) mapping. The specific surface areas of both samples (powders collected after scratch

removal) were obtained from N_2 physisorption measurements at 77 K using the Brunauer-Emmet-Teller (BET) and Barrett-Joyner-Halenda (BJH) models. Finally, the films (area $1 \times 1\ cm^2$ with thickness ~1 μm) were employed as NO_2 and H_2 gas sensors.

2.3. Sensor measurements

The gas sensor unit was made up of a stainless-steel cylindrical chamber with 250 mL volume capacity. The cylindrical chamber was with heater and PID controller to set the desired temperature. A voltage stabilizer was used to provide constant voltage to avoid the fluctuations in the temperature. The change in resistance of the sensor, due to the presence of target gas, was recorded by using Computer assisted 6-digit Keithley 6514 System electrometer. Keithley electrometer was coupled to the computer *via* RS232 interface to record the change in resistance with respect to time. For gas sensor studies, pellets of 1.5 cm (diameter) and 0.5 cm (thick- ness) area were prepared using a hydraulic pressing machine. For electrical contacts silver paste, on the sensor pellet, was

$$S(\%) = \frac{R_a - R_g}{R_a} \times 100 \qquad (1)$$

preferred. The target gases used in the experiments were obtained (Cryo gases Pvt. Ltd., Mumbai, India) in 0.5 L canisters with each of 1000 ppm concentration capacity. The gas response was calculated from the following relation;

where, R_a is the stabilized resistance of the sensor material in presence of air, R_g is the stabilized resistance in presence of the target gas.

3. Results and discussion

3.1. Structure and morphology

The phase structure, crystallinity and purity of the as-obtained BFO and BWFO film sensors were examined by XRD spectra. The strong reflections in the patterns of Fig. 1(a) are assigned to (101), (012/110), (003), (202), (113), (104), (300), (024), (220), (015), (303), and (312) lattice planes of BFO *i.e*. $BiFeO_3$ [JCPDS card no. 20-0169], and the (210), (310), (001), (400), (410), (221), (321), (401), (411), (440), (511), (540), (630), (611), (650), (412/800), and (820) lattice planes for BWFO *i.e*. $BiFeWO_6$ [JCPDS card no. 38-1289]. Other phases, than expected, to support the synthesis of different ferrite crystal structure are missing. Both materials demonstrate high crystallinity and are classed as rhombohedral type which belongs to the R3c space group. Fig. 1(b) shows the FT- IR spectra of the BFO and BWFO powders, which were measured on scratching powders off from the respective films. In both samples, at 3500 cm^{-1}, broad peaks are noticed. The BFO and BWFO reveal entirely different signatures. The EDX measurements were used to examine the surface elementals over BFO and BWFO product surfaces, whose details are shown in Fig. 1(c, d). The BFO product is composed of Bi (32.12%), Fe (16.28%), and O (51.60%), whereas on the other side, the presence of W along with the Bi (12.74%), Fe (11.59%), and O (54.56%), elements is evidencing BWFO formation whose wt.% is 20.50%. To examine the porosity distributions of the BFO and BWFO products, the N_2 adsorption-desorption isotherms were obtained from the BJH pore-size distribution spectra. As shown in Fig. 2(a, b), the N_2 adsorption and desorption spectra follow a type IV isotherm with a hysteresis loop in the relative (p/p_o) range of 10–100, which indicates the presence of mesoporous 10–50 nm in size. In addition, the hysteresis loop has shifted to a higher pressure upon approaching p/p_o ~100, suggesting a microporous and mesoporous substructures in both samples [50]. Briefly, the BFO and BWFO products are defined by BET surface areas of 5.0386 m^2/g and 8.0814 m^2/g, respectively. The pore-size distributions (insets) confirm a peak at 7.04 nm for the BFO product and two peaks at 16.10 nm and 33.04 nm for the BWFO product.

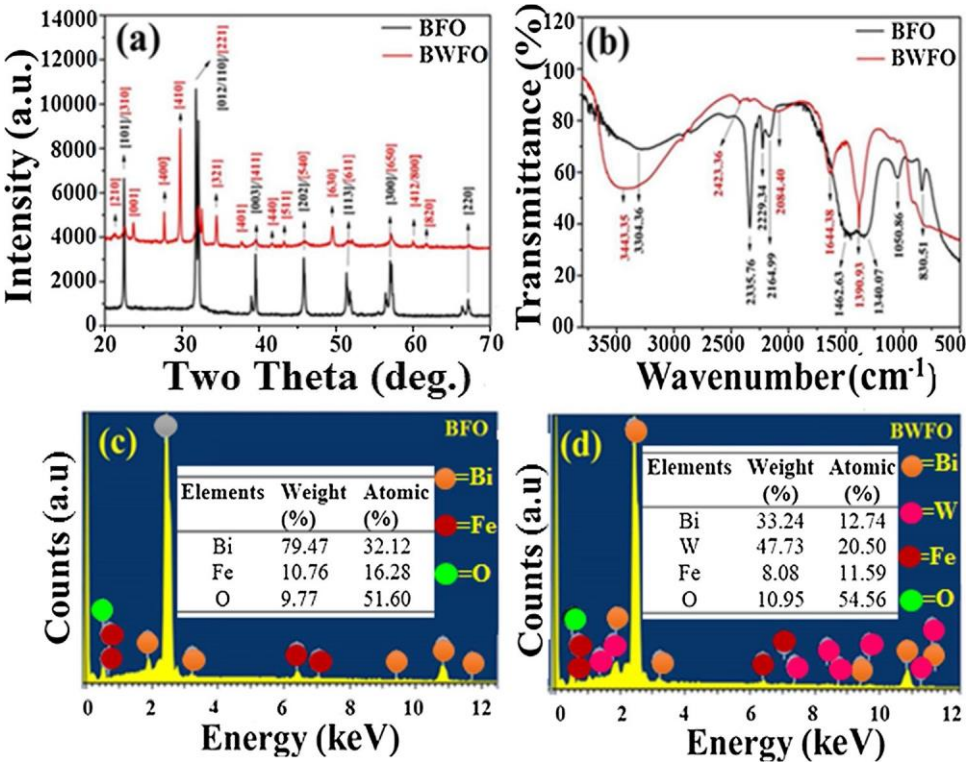

Fig. 1. (a) XRD, (b) FTIR and (c, d) EDX measurements of the sprayed BFO and BWFO films.

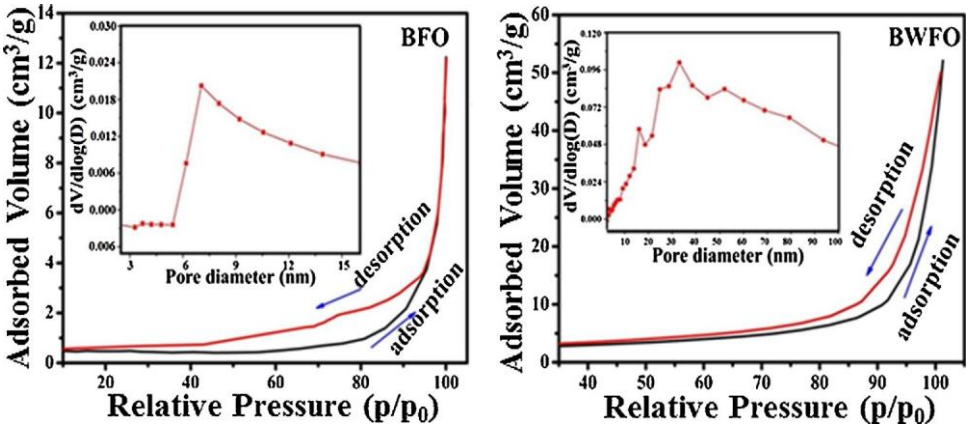

Fig. 2. N_2 adsorption-desorption isotherms and Barrett-Joyner-Halenda (BJH) pore-size distribution curves (inset) of (a) BFO and (b) BWFO nanostructures.

These pores presumably arise from the spaces among the nanostructures within the BFO and BWFO structures. The BWFO produces a higher surface-to-volume ratio than BFO which can enhance the interaction between the sensor surface and gas molecules, and the gas diffusion kinetics on the sensor surface.

The morphologies of BFO and BWFO were confirmed from the FE-SEM digital images and the results are shown in Fig. 3(a–d). The BFO film shows a uniformly distributed cluster-type morphology [Fig. 3(a, b)], and on W-doping, this morphology changes to a nanoplate-type [Fig. 3(c, d)]. The change in the morphology is due to the planar morphology of W in contrast to rounded BFO. With reference to literature data, this type of morphology is more suitable for high sensitivity due to its better adsorption rate of target gas molecules. In particular, the images confirm that the surfaces of both samples are distinct and considerably separated with moderate crevices. The surface architecture of BFO is uniform throughout but the BWFO film surface shows a combination of particle and plate type morphologies.

3.2. *Gas sensors*

3.2.1. *Sensor activities*

Fig. 4(a) shows the variation of electrical resistance of the BFO and BWFO films, which are of typically *p*-type in nature [51]. The resistivity in both films decreases linearly with operational temperature. From the curves, after tungsten doping, the resistance of BFO decreases to 0.3 M*2*. To test the gas sensing abilities and performances of the BFO and BWFO films, the gas sensor chamber was specially fabricated. Initially, the response of the sensors was measured for 100 ppm target gas and the temperature was varied between 30–250 °C for confirming the optimal operation temperature. In addition, the response and recovery times, and gas concentration effect were determined. The gas concentration was controlled by injecting a volume of gas and the chamber was purged with air to recover the sensor resistance. The sensor sensitivity was obtained from the following equations for oxidized gas (2) and reduced gas (3);

$$\textbf{Gas sensitivity}\ (\%) = \frac{\mathbf{R_a} - \mathbf{R_g}}{\mathbf{R_a}} \times 100 \qquad (2)$$

$$\textbf{Gas sensitivity}\ (\%) = \frac{\mathbf{R_g} - \mathbf{R_a}}{\mathbf{R_g}} \times 100 \qquad (3)$$

where R_a is the sensor resistance in air and R_g is the sensor resistance in the presence of gas.

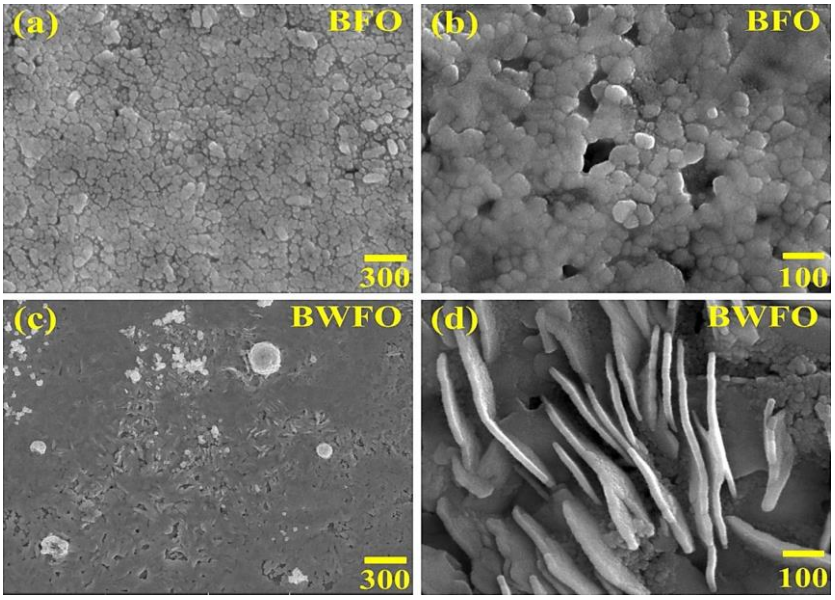

Fig. 3. (a, c) Low, and (b, d) high-magnification FE-SEM images of BFO and BWFO nanostructures.

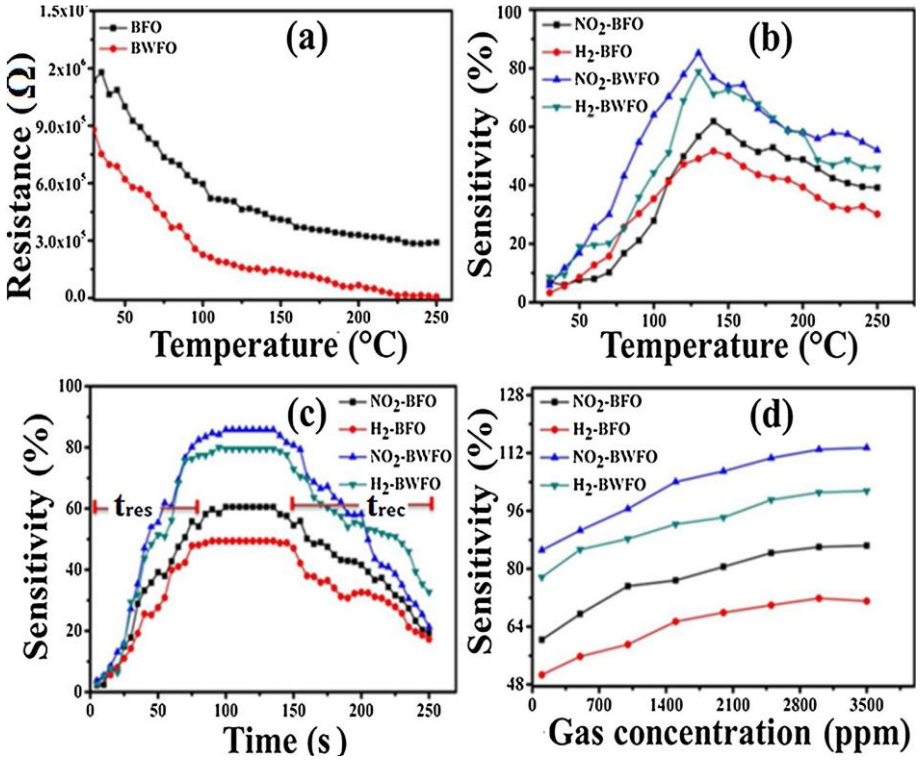

Fig. 4. (a) Resistance-temperature, (b) temperature dependence of gas response at a fixed gas concentration, (c) response and recovery, (d) responses *vs.* gas concentration measurements of the BFO and BWFO nanostructures.

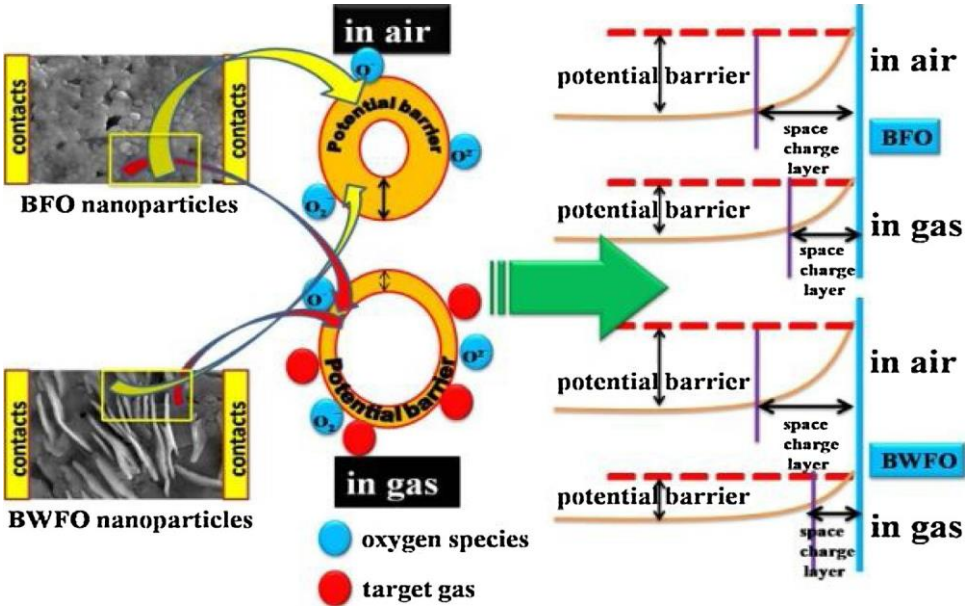

Fig. 5. Schematic presentation of NO_2 gas sensing mechanism over of the BFO and BWFO nanostructure surfaces (for H_2 it is reverse).

3.2.2. *Effect of W-doping on sensor*

Due to the catalytic effect of the W, the gas sensing performance of BFO can be significantly improved on W-doping that forms BWFO nanoplates. In general, gas sensing with metal oxide nanoparticles relies upon the interaction of the target gas with the adsorbed oxy- gen on the sensor surface. In the air, oxygen adsorbs on the sensor surface according to:

$O_2 + e^- \rightarrow O_2^-$(4)

$O_2^- + e^- \rightarrow 2O^-$(5)

This reaction creates electron deficient surface by electron 'trap- ping' by the adsorbed oxygen during its reduction, increasing the electrical resistance of *p*-type oxides, widens the depletion region and the degree of band bending. Oxidative gas, such as NO_2, also adsorbs to the sensor surface to create negatively charged species per the following reaction:

$$NO_2 + e^- \rightarrow NO_2^- \quad (6)$$

$$NO_2 + O_2^- + 2e^- \rightarrow NO_2^- + 2O^- \quad (7)$$

$$NO_2 + O^- + \rightarrow NO_2^+ + 2O^- \quad (8)$$

Reactions (4)–(8) compete for the electron extracted from the sensor surface. In contrast, *p*-type BFO and BWFO materials exhibit a reduction in resistance values from a greater hole concentration caused by utilizing electrons from the negatively charged oxygen species after exposure to an oxidizing gas such as NO_2. The sensing mechanism is therefore presented for surface reactions of the NO_2target gas in reactions (6)–(8). With the introduction of a reducing (H_2) gas to the chamber, the target gas molecules react with adsorbed oxygen and because of the reaction, the product is produced and electrons are injected back to the grain, increasing the resistance of the sensor material. The reaction mechanism for H_2 is presented below:

$$O_2 + 2e^- \rightarrow 2O^- \quad (9)$$

$$H_2 + O^- \rightarrow H_2O + e^- \quad (10)$$

The optimal operating temperature of the sensors plays a key role in their sensing properties. To determine the optimal working temperatures for these products i.e. BFO and BWFO-based sensors, the responses of these sensors to 100 ppm NO_2 and H_2 gases in the dry air were examined *vs.* temperature which are shown in Fig. 4b. The BFO sensors confirm gas responses of 62% and 50% for NO_2 and H_2 gases at 140 °C. Furthermore, BWFO responses are 87% and 78% for NO_2 and H_2 gases at 130 °C, respectively. The response reduction with further increases in temperature is due to the instability of source gas molecules at higher temperature. Additionally, grain boundary annealing is not characteristics of these materials at 130 °C. Therefore, the optimal operating temperatures, 140 °C for BFO and 130 °C for BWFO, for NO_2 and H_2 gases were confirmed and the similar results attained in the rest of the studies. These results confirm that both sensors exhibit better response sensitivity to NO_2 gas than to H_2, and BWFO sensors exhibit the best NO_2 gas response because of its mesoporous character, which may provide a high surface-to-volume ratio and large surface accessibility for the NO_2 gas molecules to enter and leave easily. Sensitivity is an important factor of a chemical sensor, higher sensitivity normally permits a low detection limit [52,53].

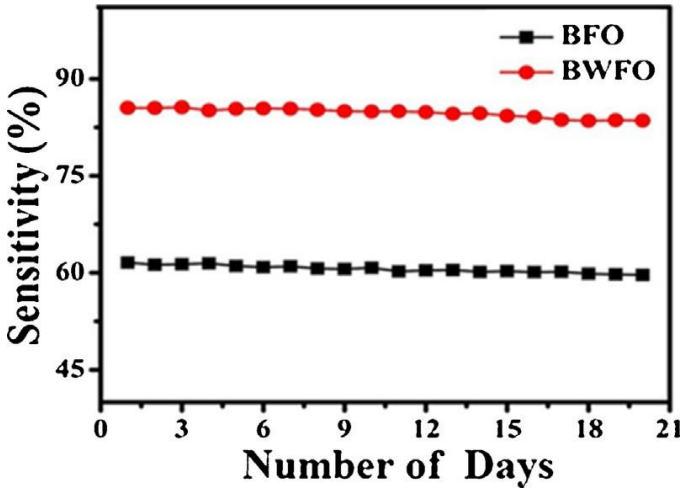

Fig. 6. NO_2 gas stability test measurements of BFO and BWFO nanostructures.

3.2.3. *Response and recovery*

In this study, the response time can be defined as the time needed for the sensor to reach 90% of the stabilized value of its sensitivity in the presence of the target gas, while the recovery time is the time needed for the sensor to reach 10% of the initial study state value of its sensitivity after the target gas removed. Based on the best gas sensing performance, the response (t_{res}) and recovery (t_{rec}) times of the BFO and BWFO sensors were determined at their optimal temperatures for 100 ppm NO_2 and H_2 gases [Fig. 4(c)]. For the BFO sensors, the response times for NO_2 and H_2 were 80 and 75 s, respectively, whereas recovery times were 100 and 105 s, respectively. The obtained response and recovery time values for the BWFO sensors were 70 and 80 s and 95 and 100 s for NO_2 and H_2, respectively. The response and recovery process is probably quickened due to the enhanced gas diffusion and the response of the sensor is probably increased because of the formation of conjugated electron depletion layers on both the outer and inner surfaces. Overall, both sensors demonstrate a sim- ilar trend in terms of the response and recovery time signatures, where the response times and recovery times are 75 s and 100 s, respectively. Fig. 4(d) shows the sensitivity of the BFO and BWFO sensors to different target gas concentrations, ranging from 100 to 3500 ppm at the optimal operating temperature; the sensitivity of the sensors increases rapidly with increasing target gas concen- tration (100–2500 ppm). Above 2500 ppm, sensitivity decreases for higher target

gas concentrations. Eventually, the sensitivity reaches to its saturation value at/above 3000 ppm. The response curves demonstrate that the sensors may detect NO_2 and H_2 gases over a wide range of concentrations, beginning with the minimum con- centration of 100 ppm and reached up to 3500 ppm. The toxic gas levels were used deliberately to determine a saturation sensitivity level. However, future work will be focused on testing the trace levels of gases for monitoring purposes.

3.2.4. *Sensing mechanism and stability*

As shown in Fig. 5, upon the introduction of NO_2 gas. The BFO sensor–support interaction results in maximum electron transportation. In this regard, the potential barrier of BFO can decrease more than the case of before gas insertion. In the next step, W is a catalyst for activating the dissociation of molecular oxygen, so electrons are produced per oxygen molecule once the gas molecules are exposed. Compared to BFO, the potential barrier of BWFO further decreases with increasing the sensitivity. In addition to the sensor response, the response and recovery times were equally important while evaluating the gas sensing mechanism. Stable performance without decay is an important measurement to evaluate the performance and consistency in sensitivity of the sensors. In Fig. 6, the long term stability measurements of BFO and BWFO sensors exposed to NO_2 and H_2 gases at 100 ppm concentration are presented. The measurements were performed over a 20 day period and the corresponding responses were recorded. No significant change in the response is evidenced, demonstrating physical stability, chemical inertness and environmental robustness of the sensors during operation.

4. Conclusions

In this study, BFO and BWFO nanostructures were synthesized by spray pyrolysis using various precursors at 400 ˚C followed air- calcination at 500 ˚C for 4 h. The XRD spectra have identified a single crystal structure of both BFO and BWFO. Surface morphology and chemical surface elemental analysis measurements have corrobo- rated change in surface appearance with anticipated stoichiometric ratios on W-doping in BFO. In addition, the as-prepared nanostructures when used as gas sensing materials to construct sensors for NO_2 and H_2, demonstrate betterr sensor performance using BWFO compared to BFO for NO_2 over H_2. These results confirm that the BWFO nanostructured films are promising sensing materials for the development of low-cost, easily-fabricated, stable and high-performance NO_2 gas sensors.

Acknowledgments

Authors extend their gratitude to University Grant Commis- sion for the financial support. This work was also supported in part by Science Foundation Ireland under grant no. 14/IA/2581. SFS would like to thank University Grants Commission, New Delhi for awarding D.S. Kothari Post-Doctoral Fellowship scheme (F.4- 2/2006 (BSR)/CH/16-17/0015).

References

[1] N. Barsan, D. Koziej, U. Weimar, Sens. Actuators B 121 (2007) 18–35.
[2] C.M. Ghimbeu, M. Lumbreras, M. Siadat, J. Schoonman, Mater. Sci. Semicond. Process. 13 (2010) 1–8.
[3] G. Cui, Z. Li, L. Gao, M. Zhang, Phys. Chem. Chem. Phys. 14 (2012) 16321–16325.
[4] B. Brunekreef, J. Expo. Sci. Environ. Epidemiol. 17 (2007) S61–S65.
[5] S. Su, W. Wu, J. Gao, J. Lub, C. Fan, J. Mater. Chem. 22 (2012) 18101–18110.
[6] D.J. Liu, T.M. Liu, H.J. Zhang, C.L. Lv, W. Zeng, J.Y. Zhang, Mater. Sci. Semicond. Process. 15 (2012) 438–444.
[7] W. Zeng, T.M. Liu, L.Y. Lin, Mater. Sci. Semicond. Process. 15 (2012) 319–325. [8] J.H. Lee, Sens. Actuators B 140 (2009) 319–336.
[9] J. Huang, Q. Wan, Sensors 9 (2009) 9903–9924.
[10] H. Zheng, J.Z. Ou, M.S. Strano, R.B. Kaner, A. Mitchell, K. Kalantar-zadeh, Adv. Funct. Mater. 21 (2011) 2175–2196.
[11] M. Yuasa, T. Kida, K. Shimanoe, ACS Appl. Mater. Interfaces 4 (2012) 4231–4236.
[12] X.j. Wang, W. Wang, Y.L. Liu, Sens. Actuators B 168 (2012) 39–45.
[13] H. Gu, Z. Wang, Y. Hu, Sensors 12 (2012) 5517–5550.
[14] M. Ahsan, T. Tesfamichael, M. Ionescu, J. Bell, N. Motta, Sens. Actuators B 162 (2012) 14–21.
[15] X. Liu, J. Zhang, L. Wang, T. Yang, X. Guo, S. Wu, S. Wang, J. Mater. Chem. 21 (2011) 349–356.
[16] M.D. Arienzo, L. Armelao, C.M. Mari, S. Polizzi, R. Ruffo, R. Scotti, F. Morazzoni, J. Am. Chem. Soc. 133 (2011) 5296–5304.
[17] C.L. Gandara, J.M.F. Sanjuan, F.M. Ramos, A. Cirera, Solid State Ionics 184 (2011) 83–87.
[18] J. Zhang, X.H. Liu, S.H. Wu, B.Q. Cao, S.H. Zheng, Sens. Actuators B 169 (2012) 61–66.
[19] D.L. Chen, X.X. Hou, T. Li, L. Yin, B.B. Fan, H.L. Wang, X.J. Li, H.L. Xu, H.X. Lu, R. Zhang, J. Sun, Sens. Actuators B 153 (2011) 373–381.
[20] Y. Zhu, X. Su, C. Yang, X. Gao, F. Xiao, J. Wang, J. Mater. Chem. 22 (2012) 13914–13917.
[21] S.J. Luo, G. Fu, H. Chen, Y.Y. Zhang, Mater. Chem. Phys. 109 (2008) 541–546.
[22] D.M. Angelo, P. Torrione, T.H. Kim, S. Wolter, W. Lampert, A. Atewologun, M. Edirisoorya, L. Collins, T.F. Kuech, M. Losurdo, G. Bruno, A. Brown, J. Phys. Chem. C 116 (2011) 826–833.
[23] L.W. Martin, Dalton Trans. 39 (2010) 10813–10826.
[24] C. Michel, J. Moreau, G.D. Achenbach, R. Gerson, W.J. James, Solid State Commun. 7 (1969) 701–704.
[25] D. Maurya, K.S. Nalwa, H. Thota, A. Garg, J. Alloys Compd. 477 (2009) 780–784. [26] M. Muneeswaran, P. Jegatheesan, N.V. Giridharan, J. Exp. Nanosci. 8 (2013) 341–346.

[27] R. Damodaran, S. Lee, J. Karthik, S.M. Laren, L.W. Martin, Phys. Rev. B 85 (2012) 024113–024117.
[28] W.J. Maeng, J.Y. Son, J. Cryst. Growth 367 (2013) 24–26.
[29] R. Guo, L. You, M. Motapothula, Z. Zhang, M.B.H. Breese, L. Chen, D. Wu, J. Wang, AIP Adv. 2 (2012) 042104–042110.
[30] R. Comes, M. Gu, M. Khokhlov, H. Liu, J. Lu, S.A. Wolf, J. Appl. Phys. 113 (2013) 023303–023309.
[31] S. Nakashima, H. Fujisawa, Y. Tsujita, S. Seto, M. Kobune, M.S. Jap, J. Appl. Phys. 51 (2012), 09LB02–09LB06.
[32] J. Wu, J. Wang, D. Xiao, J. Zhu, ACS Appl. Mater. Interfaces 4 (2012) 1182–1185. [33] L. Peng, H.M. Deng, J.J. Tian, Q. Ren, C. Peng, Z. Huang, P. Yang, J. Chu, Appl. Surf. Sci. 268 (2013) 146–150.
[34] J. Wei, D.S. Xue, Mater. Res. Bull. 43 (2008) 3368–3373.
[35] L. Wang, J.B. Xu, B. Gao, A.M. Chang, J. Chen, L. Bian, C.Y. Song, Mater. Res. Bull. 48 (2013) 383–388.
[36] T.P. Comyn, D.F. Kanguwe, J.Y. He, A.P. Brown, J. Eur. Ceram. Soc. 28 (2008) 2233–2238.
[37] Y. Liu, H. Miao, Q. Zhang, G.Q. Zhu, G.Q. Tan, Rare Met. Mater. Eng 36 (2007) 243–246.
[38] B. Li, H.J. Sun, W. Chen, Chin. J. Inorg. Chem. 25 (2009) 1848–1852.
[39] V. Koval, I. Skorvanek, M. Reece, L. Mitoseriu, H. Yan, J. Europ, Ceram. Soc. 34 (2014) 641–651.
[40] P. Sharma, D. Varshney, S. Satapathy, P.K. Gupta, Mater. Chem. Phys. 143 (2014) 629–636.
[41] P. Pandit, S. Satapathy, P.K. Gupta, V.G. Sathe, J. Appl. Phys. 106 (2009) 114105–114111.
[42] D.S. Lee, S.D. Han, J.S. Huh, D.D. Lee, Sens. Actuators B 60 (1999) 57–63.
[43] J.L. Solis, S. Saukko, L. Kish, C.G. Granqvist, V. Lantto, Thin Solid Films 391 (2001) 255–260.
[44] I. Jimenez, J. Arbiol, G. Dezanneau, A. Cornet, J.R. Morante, Sens. Actuators B 93 (2003) 475–485.
[45] V.B. O'Donnell, J.P. Eiserich, P.H. Chumley, Michael J. Jablonsky, N.R. Krishna, M. Kirk, S. Barnes, V.M.D. Usmar, B.A. Freeman, Chem. Res. Toxicol. 12 (1999) 83–92.
[46] C. Taylor, Sci. Eng. 35 (1993) 457–481.
[47] S.Y. Chiu, H.W. Huang, T.H. Huang, K.C. Liang, K.P. Liu, J.H. Tsai, W.S. Lour, Int. J. Hydrogen Energy 34 (2009) 5604–5615.
[48] W.J. Buttner, M.B. Post, R. Burgess, C. Rivkin, Int J. Hydrogen Energy 36 (2011) 2462–2470.
[49] S. Kim, G.-S. Chung, Sens. Actuators B 157 (2011) 482–486.
[50] M. Bowker, A. Nuhu, J. Soares, Catal. Today 122 (2007) 245–247.
[51] D.P. Dutta, O.D. Jayakumar, A.K. Girija, K.G. Tyagi, C.G.S. Pillai, G. Sharma, Nanoscale 2 (7) (2010) 1149–1154.
[52] J.Z. Ou, M.H. Yaacob, M. Breedon, H.D. Zheng, J.L. Campbell, K. Latham, J.D. Plessis, W. Wlodarski, K.K. Zadeh, Phys. Chem. Chem. Phys. 13 (2011) 7330–7339.
[53] J. Zhang, X.H. Liu, X.Z. Guo, S.H. Wu, S.R. Wang, Chem. Eur. J. 16 (2010) 8108–8116.